photonics

MDPI

Communication

On-Chip Tunable and Erasable Optical Waveguide Filter Using Laser-Induced Phase Transition Method

Zuming Lin [1,2,3], Xinlei Shi [1,2,3], Pengtao Zhu [1,2,3], Yiwen Xue [1,2,3], Yifeng Sun [1,2,3], Lei Gao [1,2,3], Lun Zhang [1,2,3], Yin Xu [1,2,3,*] and Hualong Bao [1,2,3,*]

1 School of Optoelectronic Science and Engineering & Collaborative Innovation Center of Suzhou Nano Science and Technology, Soochow University, Suzhou 215006, China
2 Key Lab of Advanced Optical Manufacturing Technologies of Jiangsu Province, Soochow University, Suzhou 215006, China
3 Key Lab of Modern Optical Technologies of Education Ministry of China, Soochow University, Suzhou 215006, China
* Correspondence: yinxu@suda.edu.cn (Y.X.); h.bao@suda.edu.cn (H.B.)

Abstract

Traditional tunable Bragg waveguide grating filters, which rely on thermo-optic or carrier effects, often face limitations such as high energy consumption, low tuning efficiency, and difficulty in achieving independent multi-parameter control. To overcome these bottlenecks, this work proposes a novel optical waveguide filter based on the heterogeneous integration of silicon nitride and the phase-change material Sb_2Se_3. The device leverages the substantial refractive index contrast between crystalline and amorphous states of Sb_2Se_3 to construct a programmable Bragg grating within the thin film layer. This is realized through laser-induced phase transition method, enabling nonvolatile manipulation of the light field. Simulation results indicate that the independent tuning of central wavelength over 19.2 nm range was achieved by adjusting the grating width and ripple width simultaneously. Likewise, the extinction ratio could be independently controlled over 22.3 dB through coordinated adjustments of the grating length and position shift. Beyond its tuning capabilities, the proposed device theoretically exhibits exceptional performance characteristics, including an ultra-low insertion loss of 0.1 dB and strong side lobe suppression. These advantages highlight the potential of this approach to provide a low energy consumption, multifunctional solution for integrated photonic devices, offering a promising pathway for the next generation of programmable photonic integrated circuits.

Keywords: optical waveguide filter; Bragg waveguide grating; phase change material; Sb_2Se_3; independent tuning

Check for updates

Received: 3 June 2026
Revised: 24 June 2026
Accepted: 26 June 2026
Published: 29 June 2026

Copyright: © 2026 by the authors. Licensee MDPI, Basel, Switzerland. This article is an open access article distributed under the terms and conditions of the Creative Commons Attribution (CC BY) license.

1. Introduction

The rapid growth of big data and artificial intelligence is causing wavelength division multiplexing (WDM) systems to evolve from traditional fixed architectures toward dynamic resource allocation models [1–5]. Conventional photonic integrated circuits (PICs), with their fixed functionality, struggle to meet the demands of flexible networking, such as dynamic channel scheduling and elastic bandwidth adjustment [6,7]. In contrast, reconfigurable photonic integrated circuits (RPICs) introduce dynamic control mechanisms that enable the flexible add–drop of wavelength channels, thereby significantly enhancing both transmission efficiency and networking flexibility in WDM systems [8–11].

At the heart of RPICs, integrated photonic filters play a crucial role in channel selection and wavelength routing. Various filtering structures have been proposed in recent years, including arrayed waveguide gratings (AWGs) [12,13], Mach–Zehnder interferometers (MZIs) [14,15], microring resonators (MRRs) [16,17], and Bragg waveguide gratings (WBGs) [18,19]. Among these, WBG filters stand out due to their compact size, excellent frequency selectivity, and high sensitivity to waveguide parameter variations, making them a promising candidate for on-chip filtering solutions [20,21].

For reconfigurable BWG filters, the realization of tunable filtering responses is expected to address the critical demand of key WDM components, such as optical add–drop multiplexers (OADMs) and photonic matrix–vector multipliers (PMVMs). Despite their potential advantages, most reconfigurable WBG filters rely on thermo-optic or carrier dispersion effects for spectral tuning, which are often limited by low efficiency, high loss and high energy consumption [22,23]. For instance, Cao et al. demonstrated a two-segment filter using nonlinear super-silicon-rich nitride (USRN) with a tuning range of 69–106 nm via the thermo-optic effect, but suffered from a high insertion loss of 6.35 dB [23].

To address these challenges, antimony selenide (Sb_2Se_3) has emerged as a promising low-loss phase change material. Its significant refractive index contrast ($\Delta n \approx 0.7$) and nonvolatility between crystalline and amorphous states make it particularly suitable for reconfigurable photonic devices [24]. Integrating Sb_2Se_3 with established silicon-based photonic platforms offers the potential to realize high-performance, low-power, and dynamically reconfigurable on-chip filters. For instance, Zhou et al. employed indium tin oxide (ITO) as a top heater to control a phase change material, achieving a maximum stopband center wavelength shift of 18 nm, yet independent tuning of the extinction ratio was not possible [25]. Li et al. designed a phase-shifted Bragg grating incorporating two phase change materials, allowing independent control of the band-stop wavelength (9 nm) and extinction ratio (16.1 dB) [26]. However, extinction ratio tuning introduced bandwidth changes, and the wavelength tuning range remained limited.

To address these issues, we propose a tunable optical waveguide filter based on low-loss phase change material (Sb_2Se_3). The key waveguide structure is formed by depositing an Sb_2Se_3 layer on the top surface of silicon nitride (Si_3N_4) wafer, and the corresponding optical waveguide mode is generated by refractive index difference between the amorphous and crystalline states of the Sb_2Se_3 layer and its bottom unetched silicon nitride layer. Using the laser-induced phase transition method, the phase state of Sb_2Se_3 can be locally modified, allowing the programmable construction of Bragg grating structures that can be "written" or "erased" as needed. This approach enables dynamic and independent tuning of both the center wavelength and the extinction ratio of the band-stop filter. Simulation results show a center wavelength tuning range of 19.2 nm and an extinction ratio tuning range of 22.3 dB, both of which can be independently controlled, demonstrating outstanding tuning flexibility. Regarding specific applications, the independent tunability of the proposed device allows for dynamic wavelength assignment in OADMs, while its inherent nonvolatility supports in-memory computing architectures within PMVMs. Moreover, the method simplifies the tuning process by eliminating complex electrode fabrication, significantly enhancing the practical applicability of the filter in RPICs.

2. Device Structure and Principle

Figure 1a shows the schematic of our proposed optical waveguide filter. The device consists of a Si_3N_4 wafer with a top thickness of 300 nm and a Sb_2Se_3 layer with a thickness of 50 nm deposited on it. For this filter, input (output) waveguide is a typical strip waveguide and the filtering region is patterned with periodic Bragg grating structure, where these structures are defined via the laser direct writing technique on the Sb_2Se_3 layer. The grating

has a period of Λ, and the total grating length L is designed as an integer multiple of this period. This periodic modulation of the refractive index along the waveguide transmission direction forms the fundamental mechanism for wavelength stopband filtering. Figure 1b provides a top-down magnified view of the filter, highlighting key geometrical parameters. The Bragg waveguide grating width is denoted by W, the ripple depth by W_1, the width of individual ripple by a, and the position shift of ripple on the upper and lower sides by S, respectively. Note that these parameters define the grating profile and play a critical role in determining the filtering characteristics of our proposed device.

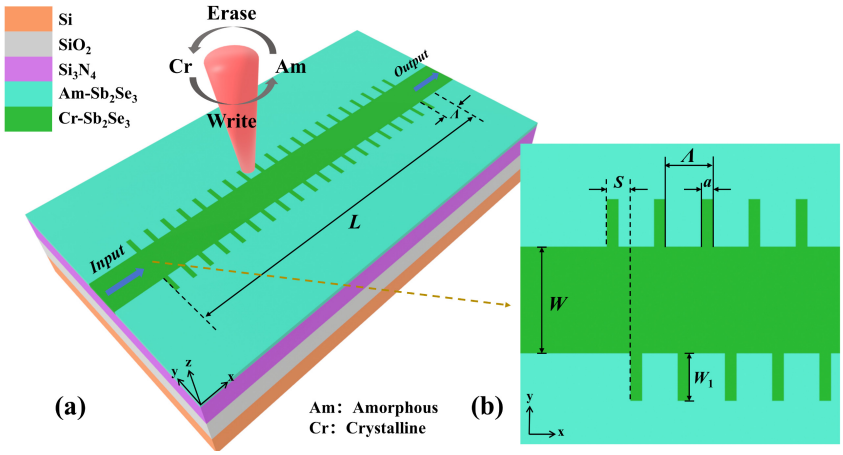


Figure 1. Device structure and key parameters. (**a**) Three-dimensional structure of our proposed optical waveguide filter, where a 50 nm thick Sb_2Se_3 layer is deposited on a 300 nm think Si_3N_4 wafer. (**b**) Top-down magnified view of the filter. Key structural parameters are labeled, e.g., grating period (Λ), total grating length (L), grating width (W), ripple depth (W_1), ripple width (a), and position shift (S), respectively.

As shown in Figure 1, the input and output waveguides are the strip waveguide, and the key filtering structure uses the Bragg waveguide grating. Note that the whole structure is fabricated via laser-induced phase transition method on the Sb_2Se_3 layer with its initial state of crystalline state (Cr-Sb_2Se_3). For the laser writing process, the designated region of the Sb_2Se_3 layer changes from a crystalline state to an amorphous state (Am-Sb_2Se_3), corresponding to the refractive index of Sb_2Se_3 decreasing from 4.012 (Cr-Sb_2Se_3) to 3.245 (Am-Sb_2Se_3) at the working wavelength of 1550 nm. In contrast, for the laser erasing process, the low-refractive-index amorphous region reverts to the crystalline region, corresponding to the restoration and resetting of the Sb_2Se_3 film state. Among them, the designated region is actually our designed device structure pattern. Using this method, we can easily change the device structure even after it has been fabricated, which means the key device structure parameters can be modified as needed. To achieve the filter function, we employ the Bragg waveguide grating structure, and the wavelength will be reflected as the Bragg reflection condition is satisfied. The Bragg reflection wavelength, λ_B, is determined by [27]

$$\lambda_B = 2n_{eff}\Lambda \quad (1)$$

where n_{eff} is the effective refractive index of the waveguide and Λ is the grating period. According to Equation (1) and flexibility of the laser-induced phase transition process on the low-loss Sb_2Se_3 layer, we can realize the dynamic adjustment of the central wavelength and extinction ratio of the stopband filter, offering flexible and precise control over the spectral response of the device.

3. Results and Discussion

In this study, two key performance metrics were analyzed: extinction ratio (ER) and insertion loss (IL), both expressed in decibels (dB). Extinction ratio quantifies the filtering strength of the device and is defined as [28]

$$\mathrm{ER} = 10\log_{10}\left(\frac{T_{\max}}{T_{\min}}\right) \tag{2}$$

where $T_{\max}$ represents the maximum transmittance within the passband, and $T_{\min}$ denotes the minimum transmittance within the stopband. Insertion loss, on the other hand, measures the optical power attenuation through the device and is defined as [28]

$$\mathrm{IL} = -10\log_{10}\left(\frac{P_{\mathrm{Output}}}{P_{\mathrm{Input}}}\right) \tag{3}$$

where P_{Output} and P_{Input} are the optical power at the output and input ports, respectively. These metrics provide a quantitative basis for evaluating the spectral performance and efficiency of the filter.

To assess the light field confinement and filtering performance of the device, three-dimensional finite-difference time-domain (3D-FDTD) simulations were performed. Figure 2 shows the electric field distribution of the input fundamental mode (TE_0) for the proposed filter. Unlike commonly used etched waveguide structures with optical modes confined within the high-refractive-index etched waveguide regions, here we employ the etchless waveguide structure and the optical mode is confined within the high-refractive-index crystalline region of the Sb_2Se_3 layer and its bottom unetched silicon nitride layer shown in Figure 2. As a contrast, such optical mode will disappear as the refractive index difference is not introduced in the Sb_2Se_3 layer. Note that we use laser-induced phase transition method to realize the phase transition between crystalline and amorphous states of the Sb_2Se_3 layer, which will be more flexible, convenient and cost-effective compared with used electrode heating phase transition.

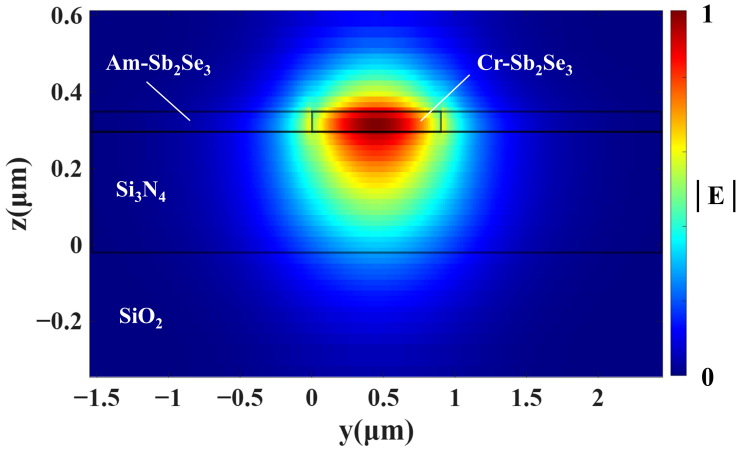


Figure 2. Simulated electric field distribution ($|\mathbf{E}|$) of input TE_0 mode for the proposed filter. Simulation shows the electric field distribution is within the high-refractive-index crystalline region of the Sb_2Se_3 layer and the underlying unetched silicon nitride layer. Black lines represent the interfaces between different materials and waveguide materials are marked.

Figure 3 presents the calculated transmission and reflection spectra of our designed optical waveguide filter. The Bragg grating in the Sb_2Se_3 layer was configured with the following structural parameters: L = 150 μm, W = 900 nm, Λ = 400 nm, W_1 = 400 nm,

a = 100 nm, and S = 0 (setting it as the reference Bragg grating structure). Under these conditions, the calculated transmission spectrum exhibits a central wavelength of 1576.5 nm and a 3 dB bandwidth of 8.6 nm, with the reflection spectrum exhibiting identical characteristics in terms of both central wavelength and bandwidth. Meanwhile, the width of central flat region in reflection spectrum is affected by five structural parameters (L, W, W_1, a, and S). According to simulation results, the device reveals excellent performance, with an ultra-low IL of approximately 0.1 dB, an ER reaching 26.1 dB, and side-mode suppression ratio in the reflection spectrum of about 4.4 dB. The pronounced notch in the transmission spectrum indicates that the Bragg grating effectively suppresses light at specific wavelengths, confirming the filtering capability of the phase-change Bragg grating formed by the laser direct writing technique on the Sb_2Se_3 layer.

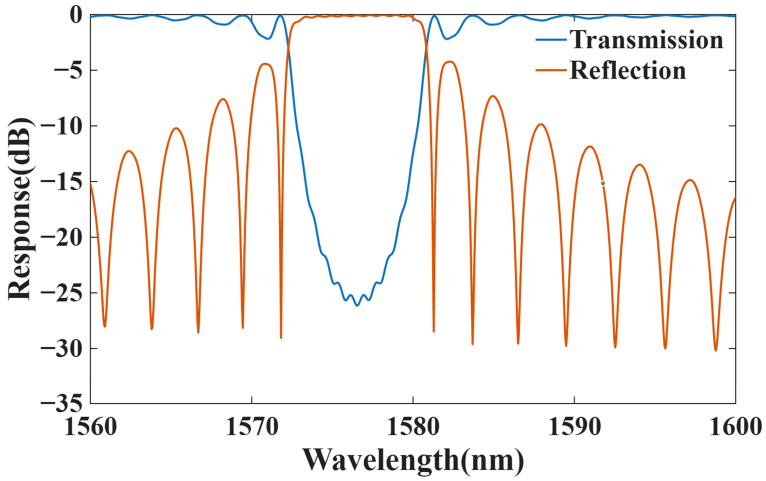


Figure 3. Calculated transmission and reflection spectra of the proposed optical waveguide filter. The device is configured with the following structural parameters: L = 150 μm, W = 900 nm, Λ = 400 nm, a = 100 nm, and S = 0, respectively.

To further analyze the filtering behavior of the device, the electric field evolution along the propagation direction was analyzed for the input TE_0 mode. In the stopband (λ = 1577 nm), the input TE_0 mode is efficiently reflected by the Bragg waveguide grating and converted into the backward-propagating TE_0 mode (which can be clearly found in Figure 4a,b). Figure 4a shows the overall reflection effect of our designed Bragg waveguide grating within its stopband and Figure 4b illustrates the distribution of the optical mode field near the interface between the input and reflective ports of the filter. In the passband (λ = 1560 nm), the input TE_0 mode can pass directly through the Bragg waveguide grating region with almost no reflection, as shown in Figure 4c,d, revealing efficient transmission at wavelengths outside the stopband. So, we can easily filter out the light within the Bragg reflection wavelength range, but this filtering range is closely related to the Bragg grating structure. Based on commonly used etched waveguide structure, this filtering range is almost impossible to further adjust after the etched waveguide structures are fabricated. Even by utilizing the electro-optic or thermal-optic effect, this filtering tunable range is very narrow. Fortunately, with the help of the laser-induced phase transition process on the low-loss phase change wafer, we can write or erase arbitrary structure pattern as needed even if the device structure has been fabricated. Therefore, we are expected to break through the limitations of traditional optical waveguide filters and achieve more flexible filtering tunable capabilities.

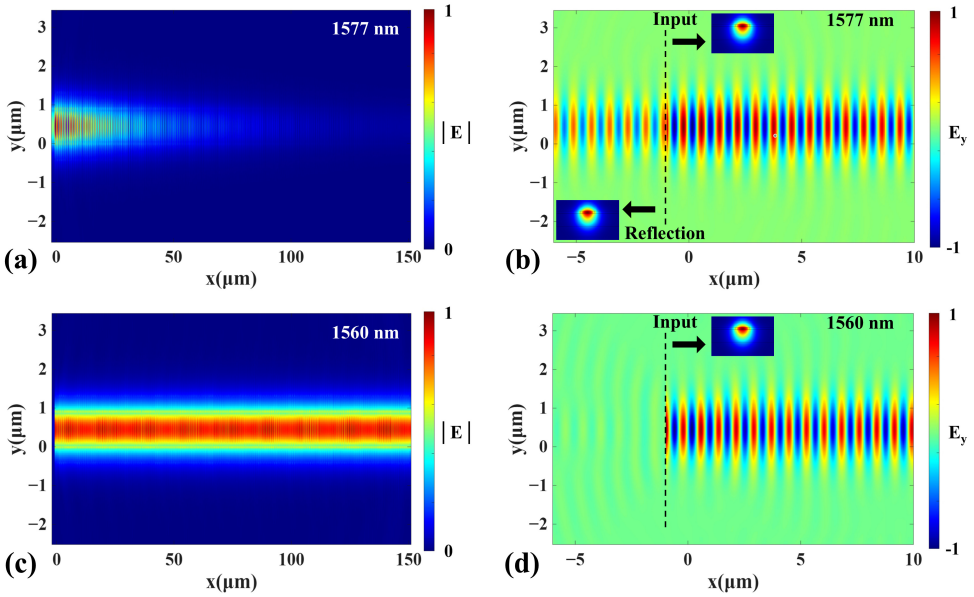


Figure 4. Electric field evolution along the propagation direction of our designed filter. (**a**) Overall electric field distribution (|**E**|) and (**b**) electric field distribution (E_y) at the interface (dotted line) between input and reflective ports in the stopband (λ = 1577 nm). (**c**) Overall electric field distribution (|**E**|) and (**d**) electric field distribution (E_y) at the interface (dotted line) between input and reflective ports in the passband (λ = 1560 nm).

Next, the key tuning capabilities of the filter were systematically investigated by analyzing the effect of each structural parameter on the filter response. Figure 5a–e show the calculated relationships between different structural parameters and filtering response.

Figure 5a shows the influence of grating length (L) on the filtering characteristics. Keeping all other parameters consistent with the reference Bragg grating structure, L was varied as 50 μm, 100 μm, 150 μm, and 170 μm. As L increased from 50 μm to 170 μm, the central wavelength of the reflection spectrum remained essentially constant, while the extinction ratio rose from 5.3 dB to 30.2 dB and the bandwidth decreased from 9.7 nm to 8.3 nm, following an approximately linear trend. Note that the spectrum fluctuations observed at L = 150 μm and 170 μm are caused by the Fabry-Pérot (F-P) resonance effect. When light propagates through the grating region, multiple reflections occur at its front and rear faces. These reflections interfere, and the resulting constructive and destructive interference makes the spectral curve non-smooth, producing noticeable fluctuations within the stopband. As the grating length L increases, the light undergoes more round trips inside the resonant cavity, and the F-P resonance effect becomes more pronounced. In addition, simulation results also reveal that modifying L can tune the extinction ratio, with only minor changes in bandwidth.

Figure 5b illustrates the effect of grating width (W) on the filtering response. With other parameters consistent with the reference Bragg grating structure and L = 100 μm, W was adjusted to 700 nm, 800 nm, 900 nm, and 1000 nm through repeated erasing operations. Increasing W from 700 nm to 1000 nm caused the central wavelength to redshift from 1560.3 nm to 1582.2 nm, the extinction ratio to decrease from 27.4 dB to 11.2 dB, and the bandwidth to narrow from 13.1 nm to 8.0 nm, respectively. This indicates that W strongly influences both the central wavelength and extinction ratio, highlighting its excellent wavelength tunability but also revealing challenges in achieving independent parameter control.

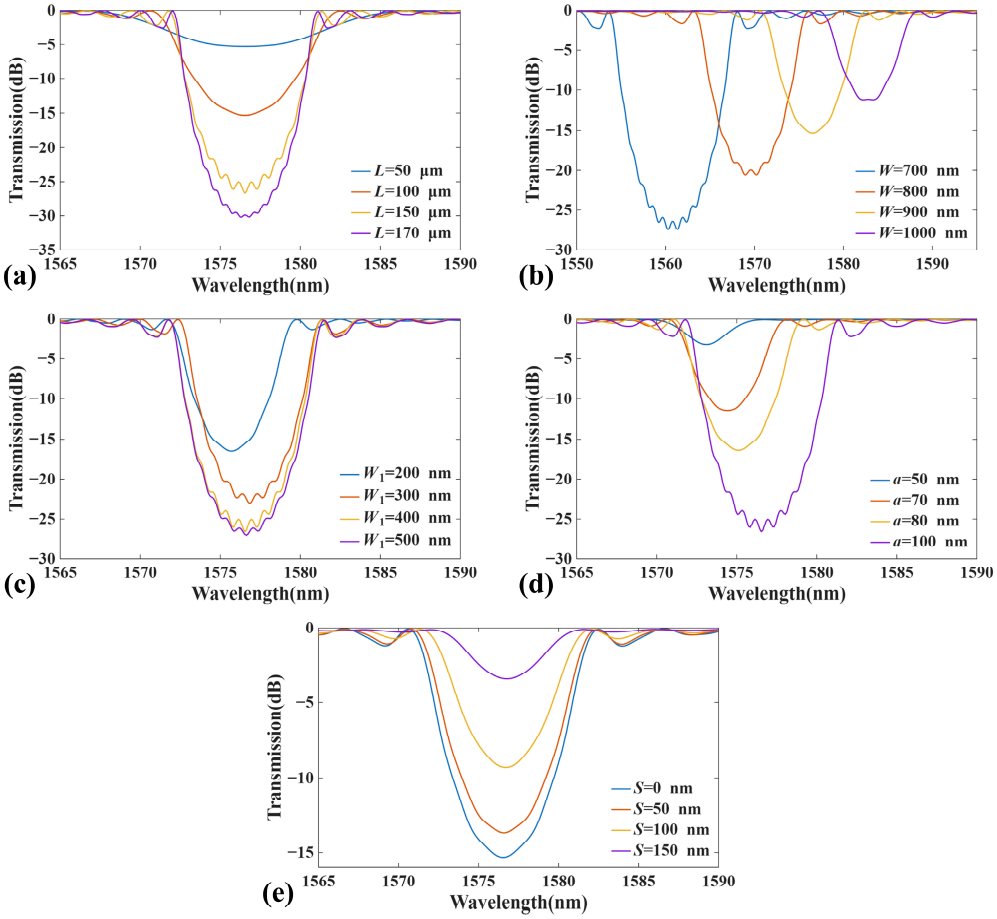


Figure 5. The calculated relationships between different structural parameters and filtering response. (**a**) Effect of grating length (*L*) from 50 μm to 170 μm. (**b**) Effect of grating width (*W*) from 700 nm to 1000 nm. (**c**) Effect of grating ripple depth (W_1) from 200 nm to 500 nm. (**d**) Effect of grating ripple width (*a*) from 50 nm to 100 nm. (**e**) Effect of grating position shift (*S*) from 0 nm to 150 nm.

Figure 5c shows the impact of grating ripple depth (W_1) on the filtering response. With other parameters consistent with the reference Bragg grating structure, W_1 was set to 200 nm, 300 nm, 400 nm, and 500 nm. As W_1 increased, the central wavelength initially redshifted from 1575.7 nm to 1576.8 nm before exhibiting a slight blueshift, the extinction ratio increased from 16.5 dB to 27.1 dB, and the bandwidth expanded from 6.5 nm to 8.7 nm, respectively. Simulation results reveal a nonlinear behavior: the changes are pronounced at first but gradually taper off as W_1 approaches 500 nm.

Figure 5d examines the effect of grating ripple width (*a*) on the filtering response. Keeping other parameters consistent with the reference Bragg grating structure, *a* was varied from 50 nm to 100 nm. As *a* increased, the central wavelength redshifted from 1573.1 nm to 1576.5 nm, the extinction ratio increased from 3.2 dB to 26.6 dB, and the bandwidth broadened from 0.9 nm to 8.8 nm, indicating that ripple width strongly affects all key spectral parameters.

Figure 5e presents the effect of the grating position shift (*S*) on the filtering response. Since simulations show symmetrical filtering behavior for *S* ranges of 0–200 nm and 200–400 nm, only the 0–200 nm range is shown. With other parameters consistent with the reference Bragg grating structure, *S* was set to 0 nm, 50 nm, 100 nm, and 150 nm. Increasing *S* caused the extinction ratio to drop from 15.3 dB to 3.4 dB and the bandwidth to shrink from 9.4 nm to 2.2 nm, while the central wavelength remained nearly unchanged. This indicates that grating position shift is highly effective for independent tuning of extinction ratio without affecting the central wavelength.

Within the study of the independent tuning of the central wavelength, it was found that variations in the grating ripple depth W_1 are difficult to effectively coordinate with other structural parameters. Therefore, W_1 is usually held constant in subsequent analyses. For the grating ripple width a, increasing its value leads to a moderate rise in both the extinction ratio and bandwidth, while the central wavelength exhibits a redshift. Although this redshift trend is similar to that observed when varying the grating width W, Figure 5d shows that the magnitude of the wavelength shift with a is smaller than that caused by changes in W. This observation suggests a strategy for independently tuning the central wavelength: by adjusting W and a simultaneously, the opposing effects on stopband bandwidth and extinction ratio can cancel each other out, leaving only the central wavelength to vary. Figure 6a shows the independent tuning of central wavelength for the proposed filter via synchronously adjusting the two parameters of W and a, where other structural parameters are set as follows: L = 100 μm, Λ = 400 nm, W_1 = 400 nm, and S = 0. As W increased from 760 nm to 1000 nm and a simultaneously increased from 74 nm to 100 nm, the central wavelength of the reflection spectrum redshifted from 1563.0 nm to 1582.2 nm, while the extinction ratio and bandwidth remained nearly constant, highlighting excellent wavelength-independent tuning capability. Moreover, the bottom of the transmission spectrum is nearly flat, which is caused by the spectrum fluctuations induced by the F-P resonance effect. Note that these structures with different parameter combinations can be realized for the single device through laser-induced phase transition technique on the Sb_2Se_3 layer. But such function cannot be realized based on a conventional etched waveguide structure for a single device.

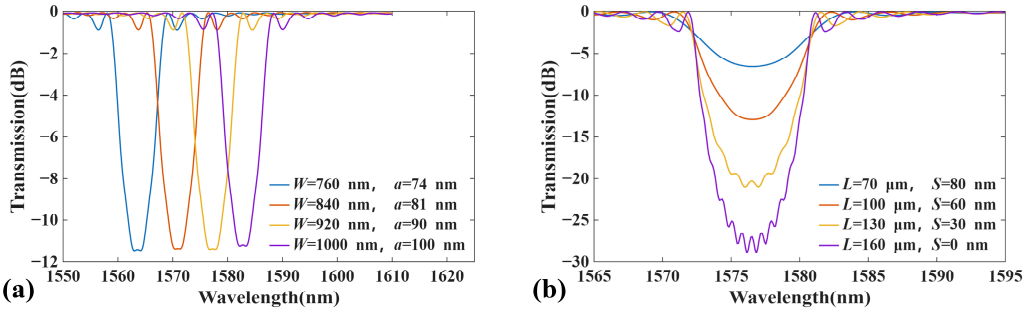


Figure 6. Simulated spectral response with independent tuning of central wavelength and extinction ratio. (**a**) Independent tuning of the central wavelength by synchronously adjusting W (from 760 nm to 1000 nm) and a (from 74 nm to 100 nm). (**b**) Independent tuning of the extinction ratio by synchronously adjusting L (from 70 μm to 160 μm) and S (from 80 nm to 0).

For independent tuning of the extinction ratio, the position shift S plays a key role. As S varies, the central wavelength of the band-stop filter remains essentially unchanged, and changes in the extinction ratio and bandwidth are positively correlated, as shown in Figure 5e. This behavior contrasts with the case of varying L, where the extinction ratio and bandwidth are negatively correlated, as shown in Figure 5a. Based on this insight, independent adjustment of the extinction ratio can be achieved by coordinating variations in both L and S: changes in the stopband bandwidth cancel each other, while the effects on the extinction ratio are additive, allowing the extinction ratio to vary independently. Figure 6b illustrates the independent tuning of extinction ratio for the proposed filter through synchronously adjusting the two parameters of L and S, where other structural parameters are set as follows: Λ = 400 nm, W = 900 nm, W_1 = 400 nm, and a = 100 nm. As L increased from 70 μm to 160 μm and S decreased from 80 nm to 0, the extinction ratio rose from approximately 6.6 dB to 28.9 dB, while the central wavelength and bandwidth remained nearly unchanged. Therefore, by adjusting multiple structural parameters simul-

taneously, the filtering wavelength and extinction ratio of our proposed device can indeed be independently tunned.

We further study the effective way to enhance the side-mode suppression ratio in the reflection spectrum of the proposed filter shown in Figure 3. Grating apodization has been proven to be an effective method for improving the side-mode suppression ratio of the reflection spectrum [29]. So, in the present Bragg grating filter, apodization is implemented by varying the position shift S along the length of the Bragg grating according to the following relationship:

$$S = \frac{\Lambda}{2}\left(1 - \exp\left(-b\frac{(x - 0.5L)^2}{L^2}\right)\right),\ 0 \le x \le L \tag{4}$$

where b is a coefficient that controls the degree of apodization, and x denotes the position along the grating with the input port as the origin. Figure 7a illustrates the schematic of the device structure with grating apodization. All other structural parameters were kept consistent with the reference Bragg grating structure, and b was set to 10. As the value of b increases, the extinction ratio of the transmission spectrum decreases, while the side-mode suppression ratio in the reflection spectrum increases gradually. So, we set b as 10 by making a trade-off between the extinction ratio and side-mode suppression ratio. Simulated transmission and reflection spectra comparing the apodized structure with the reference Bragg grating structure ($S = 0$) are shown in Figure 7b. After applying apodization, the side lobes in the transmission spectrum were almost completely eliminated, and the side-mode suppression ratio in the reflection spectrum was increased from 4.4 dB to 15.5 dB. These simulation results demonstrate that the grating apodization technique effectively suppresses side lobes in both the transmission and reflection spectra, enhancing the spectral quality of the filter.

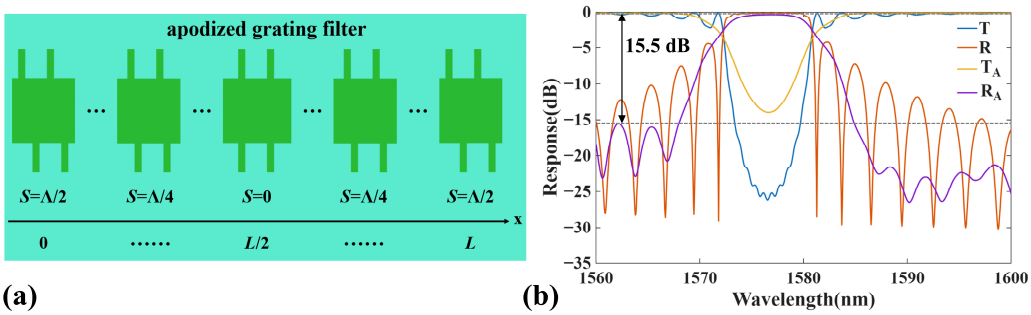


Figure 7. Grating apodization optimization. (**a**) Schematic diagram of the grating apodized structure, where the position shift S varies along the grating length. (**b**) Simulated transmission (T) and reflection (R) spectra comparing the apodized structure (A) with the reference Bragg grating structure ($S = 0$).

In order to better illustrate the performance differences between previously reported optical waveguide filters and the present one, we make a comparison table listed in Table 1 from the points of wavelength tuning range, transmission tuning range, insertion loss, footprint, tuning method, nonvolatility, and tuning independence. Through a detailed comparison, we can clearly find that the present filter has obvious advantages in the aspects of wavelength tuning range (19.2 nm), transmission tuning range (22.3 dB), insertion loss (0.1 dB), and independent tuning. In addition, using laser-induced phase transition technique, we can easily change the structure and achieve the independent tuning of central wavelength and extinction ratio of the single filter. This unique erasable feature of the present device is something that other filters based on etched optical waveguide structures cannot achieve [26,30–34]. This means that previously reported device functions are fixed once they are fabricated and their tuning ranges are intrinsically limited by the

tuning method, which nearly cannot achieve wide-range adjustment. However, the present filter can achieve relatively large-scale filtering adjustment only by changing the device structural parameters even after it is fabricated. Therefore, their tuning methods and effects are clearly different. Traditional tuning methods are based on the thermo-optic and carrier-dispersion effects, which require continuous power supply to sustain the tuned states, corresponding to high power consumption [31,33,34]. Meanwhile, phase change materials of $Ge_2Sb_2Te_5$ (GST) and $Ge_2Sb_2Se_4Te_1$ (GSST) are introduced to achieve the tunable optical waveguide filters while their relatively high material absorption loss results in a relatively high insertion loss for the device [26,30]. Note that these tuning methods require the additional fabrication of metal electrodes, which undoubtedly increases the complexity of device fabrication process. By contrast, the present filter can be easily tuned by using the laser-induced phase transition method, without the need for additional electrode fabrication. For the reconfigurability and scalability, these schemes almost all have these functions. The sole limitation of present filter in its applications is the requirement of a laser-induced phase transition system, which will be used to perform the specified phase change operations on the phase change material, and the flexibility in use is currently not as convenient and efficient as that of electrodes. Furthermore, in the present work, the reported filtering results are based on the numerical simulations and experimental characterizations are under way. We hope to obtain the experimental results of our designed tunable filter in the near future.

Table 1. Comparison between different tunable optical waveguide filters.

Reference	Wavelength Tuning Range (nm)	Transmission Tuning Range (dB)	Insertion Loss (dB)	Footprint (μm^2)	Tuning Method	Nonvolatility	Tuning Independence
[26] (S)	9	16.1	0.8	~16	Sb_2Se_3 GSST	Yes	Yes
[30] (S)	8.8	19.2	~2.6	~10	GST	Yes	No
[31] (E)	5.9	—	4/6	~375,285	Carrier-dispersion	No	Yes
[32] (E)	—	31.4	<0.5	~22	Sb_2Se_3	Yes	No
[33] (S)	~0.0014	—	<5	~1100	Thermo-optic	No	Yes
[34] (E)	~0.249	—	2.2	~1,120,000	Thermo-optic	No	Yes
This work (S)	19.2	22.3	0.1	~918	Erasable structure	Yes	Yes

E: experiment; S: simulation; "—": not mentioned.

The device fabrication part encompasses the Sb_2Se_3 film deposition and the experimental setup of phase change laser processing platform including writing and erasing effects. The procedure for the Sb_2Se_3 film deposition is illustrated in Figure 8. Specifically, a Si_3N_4 wafer serves as the substrate, and Sb_2Se_3 film is deposited on the surface of the substrate using physical vapor deposition (PVD), such as ion beam sputtering and magnetron sputtering [35,36].

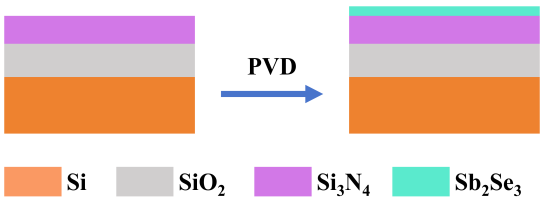


Figure 8. Procedure for Sb_2Se_3 film deposition on Si_3N_4 wafer. PVD: physical vapor deposition.

For the device fabrication, we have set up a laser-induced phase transition fabrication system, as shown in Figure 9. The fabrication system illustrated in Figure 9a includes a laser alignment and focusing optical path as well as a lighting and imaging optical path. For the former, the emitted beam from red-light solid-state laser (639 nm) is firstly modulated via

acousto-optic modulator (AOM), then passes through two beam splitters (BS1, BS2), and finally is focused on the sample surface by a 50x objective lens (numerical aperture = 0.5). As for single-spot writing, a rectangular pulse with a duration of 500 ns and power of 8.06 mW is applied. Conversely, the erasing operation utilizes a 5 ms pulse with power of 2.95 mW. For the latter, the white light from light-emitting diode (LED) first shines on the sample surface and then the reflected light passes through objective lens, BS2, BS1, filter, convex lens, and finally is captured by CCD camera for imaging display. Note that the filter is employed to suppress residual reflections from the processing laser, thereby improving imaging contrast. Using such observation and imaging structure, we can observe the fabrication situation and results of the sample in real time. In addition, the translation stage is used to move the sample, enabling the laser writing and erasing of the designed structural patterns on the Sb_2Se_3 film. Figure 9b shows the corresponding experimental setup and we will use such setup to fabricate our proposed tunable optical waveguide filter. Note that a SiO_2 capping layer has been applied to the Sb_2Se_3 surface to prevent the volatilization, thermal degradation, and oxidation of phase change material. At present, the writing accuracy of our fabrication system is about 400 nm. Further improvement depends on the shorter wavelength of writing laser and higher numerical aperture of objective lens. Moreover, Sb_2Se_3 material does not show any significant performance degradation within 100 repetitions of writing and erasing processes within our experiment. Switching speed ranges from nanosecond to millisecond, which can meet the requirements of reconfigurable applications.

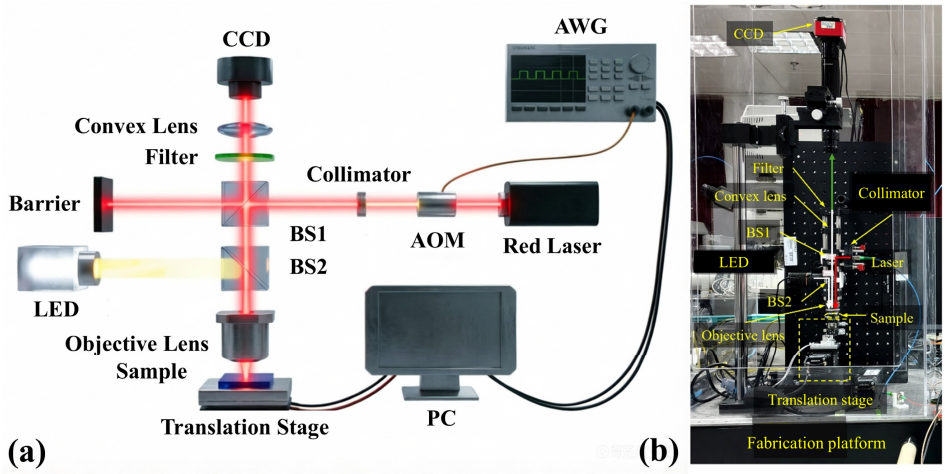


Figure 9. Fabrication system for the optical waveguide filter. (**a**) Schematic of the laser-induced phase transition fabrication system. (**b**) Experimental setup. BS: Beam splitter, AWG: arbitrary waveform generator, AOM: acoustic optical modulator, PC: personal computer, LED: light-emitting diode.

Regarding the feasibility of on-chip integration with traditional optoelectronic devices, the fabrication of the proposed reconfigurable device is fully compatible with the back-end of line (BEOL) processes standard in complementary metal-oxide semiconductor (CMOS) foundries. This compatibility is primarily enabled by the low thermal budget required for Sb_2Se_3 thin-film deposition, which can be performed at temperatures well below 400 °C—significantly lower than the threshold that would damage underlying CMOS circuitry or silicon photonic waveguides. Moreover, the utilization of laser-induced local phase transition eliminates the need for global high-temperature annealing, thereby enabling the direct monolithic integration of reconfigurable photonic functions on top of existing electronic-photonic chips without compromising yield or reliability.

For the proposed optical waveguide filter, the variability of its structure parameter is the key to achieving tunable filtering functionality for the single device. We employ our

established fabrication system shown in Figure 9 to fabricate the filter and the variability of structural parameters is also demonstrated on a single device. Two key structural parameters, the grating length (L) and ripple depth (W_1), were systematically varied, while all other parameters were kept constant. Reversible phase transitions between crystalline and amorphous states were induced through repeated writing and erasing processes, allowing the formation of Bragg gratings with different configurations. Figure 10a–f present optical images of fabricated Bragg waveguide gratings with different grating lengths L and ripple depths W_1. By considering the limitation of our CCD display range and marker lines, we take the variations in L and W_1 as examples. Variability of other filtering structure parameters can also be achieved using our fabrication system. From Figure 10, we find that the grating length and ripple depth of the filter can be easily increased or decreased on a single device without having to fabricate the devices with different structure parameters again and again. Therefore, based on the device structure described in here and the laser-induced phase transition method, we can easily change the device structural parameters even after it is fabricated. Further experimental characterizations of our proposed filter are under way.

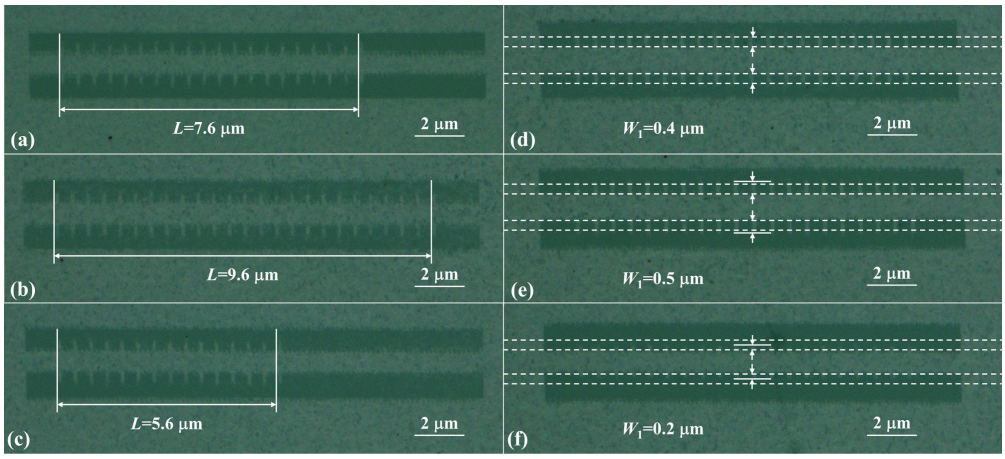


Figure 10. Optical images of fabricated Bragg waveguide gratings on a single device. The images demonstrate the reversible variation in structural parameters via laser-induced phase transition. (**a**–**c**) Gratings with different lengths: L = 7.6 μm, L = 9.6 μm, and L = 5.6 μm, respectively. (**d**–**f**) Gratings with different ripple depths: W_1 = 0.4 μm, W_1 = 0.5 μm, and W_1 = 0.2 μm, respectively.

4. Conclusions

In summary, we present a tunable optical waveguide filter based on the low-loss phase change material Sb_2Se_3. By depositing an Sb_2Se_3 layer on the silicon nitride wafer, the filtering structure pattern is formed based on the obvious refractive index difference between crystalline and amorphous states of Sb_2Se_3. Such structure pattern can be fabricated on the Sb_2Se_3 film via the laser-induced phase transition method. Simulation results reveal that independent tuning of the central wavelength over a 19.2 nm range and the extinction ratio by 22.3 dB can be achieved for the filter, including an ultra-low insertion loss of 0.1 dB. In addition, an apodization scheme is further introduced to improve filtering performance, increasing the side-mode suppression ratio in the reflection spectrum from 4.4 dB to 15.5 dB. Meanwhile, the structure of the proposed filter is erasable even after it is fabricated, where such function cannot be realized for current etched optical waveguide devices. Based upon the features of nonvolatility, erasability, and flexible independent tunability, we hope such a scheme and device could find potential applications in the reconfigurable and programmable photonic integrated circuits to address the issues of dynamic wavelength selection and filtering.

Author Contributions: Conceptualization, Z.L.; methodology, Z.L., X.S., P.Z. and Y.X. (Yiwen Xue), Y.S., L.G., L.Z. and Y.X. (Yin Xu); investigation, Z.L. and Y.X. (Yin Xu); writing—original draft preparation, Z.L. and Y.X. (Yin Xu); writing—review and editing, all authors; supervision, Y.X. (Yin Xu); project administration, Y.X. (Yin Xu) and H.B. All authors have read and agreed to the published version of the manuscript.

Funding: This research was funded by National Natural Science Foundation of China, grant number 62205129, and Research Foundation of Engineering Research Center of Digital Imaging and Display, Ministry of Education, Soochow University, grant number ZZ2402.

Institutional Review Board Statement: Not applicable.

Informed Consent Statement: Not applicable.

Data Availability Statement: The data that support the findings of this study are available from the corresponding authors upon reasonable request.

Conflicts of Interest: The authors declare no conflicts of interest.

References

1. Liu, Z.; Xu, Y.; Chen, S.; Zhu, X.; Wang, S.; Chu, S.T.; Little, B.E.; Morandotti, R.; Moss, D.J.; Bai, Y.; et al. Interleaved soliton-crystal microcombs for dense wavelength-division multiplexing technology. *Acta Opt. Sin.* **2026**, *46*, 0700011.
2. Zhang, Y.; Wang, C.; Sang, B.; Zhang, Y.; Wang, X.; Zhou, W.; Yu, J. 16QAM mode-wavelength division multiplexing coherent transmission system based on MIMO neural network equalization. *Acta Opt. Sin.* **2024**, *44*, 0306003.
3. Jung, S.-Y.; Kang, E.K.; Kwon, W.-B.; Kwon, S.; Kim, M.; Cho, G.-S.; Kang, H.C.; Moon, D.W.; Yun, S.-J.; Han, Y.-T.; et al. 8-λ LAN-WDM TOSA for 800-Gb/s links with simplified, non-hermetic packaging. *Opt. Express* **2026**, *34*, 11259–11270. [PubMed]
4. Jin, K. Evolution of Optical Network Paradigms: From Elastic and Software-Defined Architectures to All-Photonic 6G Systems. Available online: http://www.cse.wustl.edu/ jain/cse5700-25/ftp/apn/index.html (accessed on 22 May 2026).
5. Doherty, M.; Matzner, R.; Sadeghi, R.; Bayvel, P.; Beghelli, A. Reinforcement learning for dynamic resource allocation in optical networks: Hype or hope? *J. Opt. Commun. Netw.* **2025**, *17*, 1943–2025. [CrossRef]
6. Morichetti, F.; Milanizadeh, M.; Petrini, M.; Zanetto, F.; Ferrari, G.; de Aguiar, D.O.; Guglielmi, E.; Sampietro, M.; Melloni, A. Polarization-transparent silicon photonic add-drop multiplexer with wideband hitless tuneability. *Nat. Commun.* **2021**, *12*, 4324. [PubMed]
7. Yazdani, H.; Raz, O.; Abdel-Aal, O. Programmable and Reconfigurable Photonic Integrated Circuits. Available online: https://doi.org/10.5772/intechopen.1011841 (accessed on 22 May 2026).
8. Wu, J.; Cao, P.; Pan, T.; Yang, Y.; Qiu, C.; Tremblay, C.; Su, Y. Compact on-chip 1 × 2 wavelength selective switch based on silicon microring resonator with nested pairs of subrings. *Photon. Res.* **2015**, *3*, 9–14.
9. Yang, M.; Wang, T.; Liang, Y.; Jin, Y.; Zhang, W.; Meng, X.; Li, A.; Zhang, G.J.; Li, W.; Shi, N.; et al. Scalable and rapid programmable photonic integrated circuits empowered by Ising-model intelligent computation. *Photon. Res.* **2025**, *13*, 1832–1842. [CrossRef]
10. Liu, H.; Pan, B.; Li, H.; Yu, Z.; Liu, L.; Shi, Y.; Dai, D. First demonstration of lithium niobate photonic chip for dense wavelength-division multiplexing transmitters. *Adv. Photon.* **2024**, *6*, 066001. [CrossRef]
11. Mori, Y.; Honda, E.; Shiraki, R.; Suzuki, K.; Matsuura, H.; Kawashima, H.; Namiki, S.; Ikeda, K.; Sato, K.-I. Wavelength-division demultiplexing enhanced by silicon-photonic tunable filters in ultra-wideband optical-path networks. *J. Light. Technol.* **2020**, *38*, 1003–1007.
12. Pan, P.; An, J.; Wang, Y.; Zhang, J.; Wang, L.; Qi, Y.; Han, Q.; Hu, X. Compact 4-channel AWGs for CWDM and LAN WDM in data center monolithic applications. *Opt. Laser Technol.* **2015**, *75*, 177–181. [CrossRef]
13. Goldstein, N.; Pascar, L.; Sinefeld, D.; Golani, O.; Marom, D.M. Fine resolution spectral filtering using a 25 GHz free-spectral range arrayed waveguide grating. In Proceedings of the Optical Fiber Communication Conference (OFC), Los Angeles, CA, USA, 22–26 March 2015.
14. Xing, P.; Viegas, J. Broadband CMOS-compatible SOI temperature insensitive Mach-Zehnder interferometer. *Opt. Express* **2015**, *23*, 24098–24107. [PubMed]
15. Lee, J.-M.; Kim, M.-S.; Ahn, J.T.; Adelmini, L.; Fowler, D.; Kopp, C.; Oton, C.J.; Testa, F. Demonstration and fabrication tolerance study of temperature-insensitive silicon-photonic MZI tunable by a metal heater. *J. Light. Technol.* **2017**, *35*, 4904–4908.
16. Tan, Y.; Chen, S.; Dai, D. Polarization-selective microring resonators. *Opt. Express* **2017**, *25*, 4106–4119. [CrossRef] [PubMed]
17. Dahlem, M.S.; Holzwarth, C.W.; Khilo, A.; Kärtner, F.X.; Smith, H.I.; Ippen, E.P. Reconfigurable multi-channel second-order silicon microring-resonator filterbanks for on-chip WDM systems. *Opt. Express* **2011**, *19*, 306–316. [PubMed]

18. Yao, J.; Zhang, W. Fully reconfigurable waveguide Bragg gratings for programmable photonic signal processing. *J. Light. Technol.* **2020**, *38*, 202–212. [CrossRef]
19. Falconi, F.; Porzi, C.; Sharp, G.J.; Bogoni, A.; Sorel, M. Widely tunable silicon photonics narrow-linewidth passband filter based on phase-shifted waveguide Bragg grating. In Proceedings of the 2018 IEEE 15th International Conference on Group IV Photonics (GFP), Cancun, Mexico, 29–31 August 2018.
20. Yin, S.-Y.; Guo, Q.; Liu, S.-R.; He, J.-W.; Yu, Y.-S.; Tian, Z.-N.; Chen, Q.-D. Three-dimensional multichannel waveguide grating filters. *Opto-Electron. Sci.* **2024**, *3*, 240003. [CrossRef]
21. Zhao, Y.; Shi, Y.; Chen, Y.; Liu, S.; Dai, P.; Liu, G.; Ni, Y.; Chen, X. Compact and wideband silicon optical channel-drop filter based on dual-strip waveguide antisymmetric Bragg gratings. *Opt. Lett.* **2025**, *50*, 2417–2420. [PubMed]
22. Soref, R.A.; De Leonardis, F.; Passaro, V.M.N. Scanning spectrometer-on-a-chip using thermo-optical spike-filters or Vernier-comb filters. *J. Light. Technol.* **2019**, *37*, 3194–3198.
23. Cao, Y.; Isahin, E.; Choi, J.W.; Xing, P.; Chen, G.F.R.; Ng, D.K.T.; Eggleton, B.J.; Tan, D.T.H. Thermo-optically tunable spectral broadening in a nonlinear ultra-silicon-rich nitride Bragg grating. *Photon. Res.* **2021**, *9*, 596–604.
24. Delaney, M.; Zeimpekis, I.; Lawson, D.; Hewak, D.W.; Muskens, O.L. A new family of ultralow loss reversible phase-change materials for photonic integrated circuits: Sb_2S_3 and Sb_2Se_3. *Adv. Funct. Mater.* **2020**, *30*, 2002447.
25. Zhou, T.; Gao, Y.; Wang, G.; Chen, Y.; Gu, C.; Bai, G.; Shi, Y.; Shen, X. Reconfigurable hybrid silicon waveguide Bragg filter using ultralow-loss phase-change material. *Appl. Opt.* **2022**, *61*, 1660–1665. [PubMed]
26. Li, W.; Qiu, C.; Wu, A. Nonvolatile reconfigurable phase-shifted Bragg grating filter with tunable wavelength and extinction ratio. *IEEE Photonics J.* **2023**, *15*, 2200707. [CrossRef]
27. Alquliah, A.; Sun, J.K.C.; Mekhiel, C.; Gao, C.; Gulinihali, G.; Fainman, Y.; Ndao, A. Electrically reconfigurable non-volatile on-chip Bragg filter with multilevel operation. *Nanophotonics* **2023**, *12*, 2400165.
28. Chen, C.-H.; Pang, L.; Tsai, C.-H.; Levy, U.; Fainman, Y. Compact and integrated TM-pass waveguide polarizer with a subwavelength-wide slot. *Opt. Express* **2005**, *13*, 5347–5352. [PubMed]
29. Li, T.; Pu, Y.; Zheng, S.; Qiu, Y.; Zhao, X.; Zhong, Q.; Dong, Y.; Hu, T. Study and design of polarization-insensitive narrow-band apodized grating filters. *Study Opt. Commun.* **2025**, *3*, 240067.
30. Badri, S.H.; Gilarlue, M.M.; Farkoush, S.G.; Rhee, S.-B. Reconfigurable bandpass optical filters based on subwavelength grating waveguides with a $Ge_2Sb_2Te_5$ cavity. *J. Opt. Soc. Am. B* **2021**, *38*, 1283–1287.
31. Xie, L.; Chen, L.R. Bandwidth-variable and wavelength-tunable waveguide Bragg grating filter. *IEEE Photonics J.* **2025**, *17*, 6601206.
32. Sun, B.; Wei, M.; Lei, K.; Chen, Z.; Sun, C.; Li, J.; Li, L.; Lin, H. Integrated Bragg grating filters based on silicon-Sb_2Se_3 with non-volatile bandgap engineering capability. *Opt. Express* **2023**, *31*, 27905–27913. [PubMed]
33. Toma, A.; Brunetti, G.; Saha, N.; Ciminelli, C. Fully reconfigurable photonic filter for flexible payloads. *Appl. Sci.* **2024**, *14*, 488. [CrossRef]
34. Shawon, M.J.; Saxena, V. Fully automatic in-situ reconfiguration of optical filters in a CMOS-compatible silicon photonic process. *J. Light. Technol.* **2023**, *41*, 1286–1297.
35. Chen, R.; Fang, Z.; Fröch, J.E.; Xu, P.; Zheng, J.; Majumdar, A. Broadband Nonvolatile Electrically Controlled Programmable Units in Silicon Photonics. *ACS Photonics* **2022**, *9*, 2142–2150. [CrossRef]
36. Zheng, J.; Fang, Z.; Wu, C.; Zhu, S.; Xu, P.; Doylend, J.K.; Deshmukh, S.; Pop, E.; Dunham, S.; Li, M.; et al. Nonvolatile Electrically Reconfigurable Integrated Photonic Switch Enabled by a Silicon PIN Diode Heater. *Adv. Mater.* **2020**, *32*, 2001218. [CrossRef]

Disclaimer/Publisher's Note: The statements, opinions and data contained in all publications are solely those of the individual author(s) and contributor(s) and not of MDPI and/or the editor(s). MDPI and/or the editor(s) disclaim responsibility for any injury to people or property resulting from any ideas, methods, instructions or products referred to in the content.